The 15th International Symposium on Magnetic Bearings, August 3-6, 2016, Mojiko Hotel, Kitakyushu, Japan

ISMB15

Basic Calculation of Axial Force and Torque with Permeance Method in One-Axis Actively Positioned Single-Drive Bearingless Motor

Itsuki SHIMURA*, Hiroya SUGIMOTO* and Akira CHIBA*

*Depertment of Electrical and Electronic Engineering, Tokyo Institute of Technology

2-12-2 Ookayama, Meguro, Tokyo 152-8550, Japan

E-mail: shimura.i@belm.ee.titech.ac.jp

Abstract

This paper presents mathematical calculations of active axial force and torque in a single-drive bearingless motor. The single-drive bearingless motor has only one set of three-phase winding. The active axial force and torque are generated by *d*- and *q*-axis currents, respectively. Only the rotor axial *z*-axis position is actively regulated. The other axes, radial movements *x* and *y*, and tilting movements θ_x and θ_y are passively stabilized. In this paper, the mathematical equations of the active axial force and torque based on a permeance method are derived. It is confirmed that calculated force and torque are corresponding with those of three-dimensional finite-element-method analysis.

Keywords : bearingless motor, magnetic bearing, single-drive, one degree-of-freedom, permanent magnet motor

1. Introduction

Bearingless motors have advantages of no wear, no lubricant, non-pollution and maintenance-free because a magnetic bearing function is magnetically integrated in a single motor. As a result, the bearingless motors have been applied in centrifugal pumps, contamination-free ventricular assist devices, high purity pharmaceutical mixing devices, rotating stages and flywheels.

In recent studies of the magnetically suspended motors, the number of actively regulated axes is reduced because of the cost reduction. In one-axis actively positioned magnetic bearing motors and bearingless motors [1]-[8] only one degree of freedom (1DOF) is actively regulated, i.e., only the axial direction *z* is actively positioned, thus, only one displacement sensor and two or less number of inverters are necessary. The other axes are passively stabilized by passive magnetic bearing functions. Therefore, the cost is reduced with respect to 5DOF or 2DOF actively positioned bearingless motors. In particular, a few single-drive bearingless motors with 1DOF active positioning can generate both torque and suspension force with only one three-phase inverter [6]-[8]. Therefore, the cost can be reduced further. The authors have studied a 1DOF actively positioned single-drive bearingless motor for cooling fan application [7]-[8].

This paper presents equivalent magnetic circuits of the proposed single-drive bearingless motor. The mathematical equations of the active axial force and torque are derived. In addition, it is found that the proposed mathematical equations are effective to approximate the axial suspension force and torque.

2. Proposed Machine Structure

Fig. 1 shows the prototype machine structure in [8]. The machine is composed of a single-drive bearingless motor and two repulsive passive magnetic bearings. In the center, the stator and the rotor consist of three layers. In the center layer, the active axial force and the rotational torque are generated. In the upper and lower layers, only active axial force is generated. The center stator employs the laminated silicon steel and the upper and lower stator cores employs the soft magnetic composite. The upper and lower stator cores are bent to extend slot area in *xz* cross-sectional view. Therefore, supplemental windings can be installed around the upper and lower stator cores. The stator slot area is increased by three-dimensional tooth structure thanks to the soft magnetic composite. As a result, the axial active force is improved because

the number of windings is increased. The rotor has permanent magnets (PMs) for eight rotor poles, and the magnetized directions in the center and lower layers are the identical. In contrast, the magnetized direction in the upper rotor is opposite to the other layers.

Fig. 2 shows *xy* cross-sectional view. Only center layer is illustrated. The stator has twelve teeth and three-phase eight-pole windings. The rotor PMs are inserted in a paramagnetic PM holder. Thus, the rotor is a typical surface permanent magnet (SPM) rotor. The rotor outer diameter, magnetic gap, and mechanical gap are 27.4 mm, 0.8 mm, and 0.3 mm, respectively.

Fig. 3 shows the flux density distribution when the positive *d*-axis current of 6.12 A is provided. The rotor rotational angular position in Fig. 3 is corresponding to the *d*-axis. Black arrows indicate the magnetized direction of the PMs. The upper and lower PMs causes fluxes in the *z*-axis direction because the PMs are installed at unaligned positions with respect to the stator teeth. When the *d*-axis current is positive, the flux densities in the air-gap g_1 and g_3 are increased because the PM and the suspension fluxes are intensified. On the other hand, the flux densities in the air-gap g_2 and g_4 are weakened. As a result, the positive axial force is generated. In case of negative *d*-axis current, negative axial force is generated.

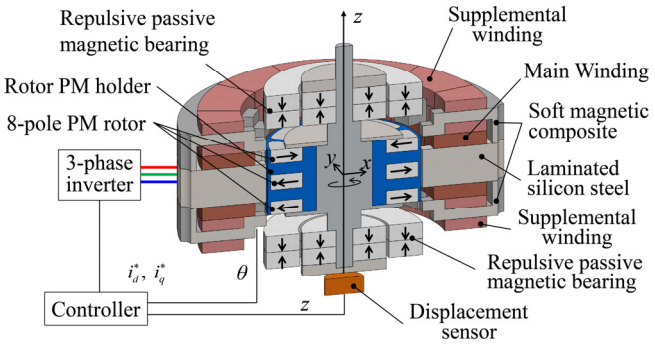

Fig. 1. Proposed structure.

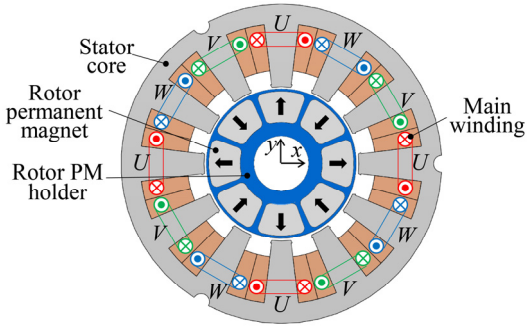

Fig. 2. *xy* cross-sectional view of proposed structure.

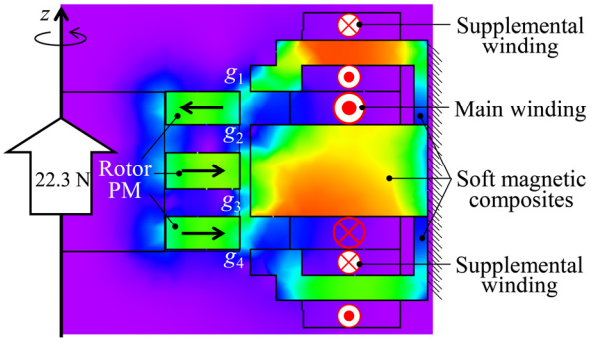

Fig. 3. Principle of active axil force generation.

2. Voltage Equation

In [8], the voltage equation has been derived. Let us define v_d and v_q as *d*- and *q*-axis voltages, respectively, *R* and *L* as a winding resistance and an inductance per phase, respectively, and an electrical angular speed as ω_e. Let us also define Ψ_ω and Ψ'_z as a flux linkage at axial displacement $z = 0$ and a flux linkage per axial displacement *z*, respectively. The voltage equation is given as

$$\begin{bmatrix} v_d \\ v_q \end{bmatrix} = \begin{bmatrix} R + \frac{\mathrm{d}}{\mathrm{dt}}\frac{3}{2}L & -\omega_e \frac{3}{2}L \\ \omega_e \frac{3}{2}L & R + \frac{\mathrm{d}}{\mathrm{dt}}\frac{3}{2}L \end{bmatrix} \begin{bmatrix} i_d \\ i_q \end{bmatrix} + \begin{bmatrix} \frac{\mathrm{d}z}{\mathrm{dt}}\Psi'_z \\ \omega_e \Psi_\omega (1 + k_\omega z) \end{bmatrix}, \tag{1}$$

where, k_ω is a coefficient of variation of induced voltage due to the rotor axial displacement. The torque *T* and the axial suspension force F_z can be expressed using voltage equation parameters and number of pole pairs *p* as,

$$T = p\Psi_\omega (1 + k_\omega z) i_q \tag{2}$$

$$F_z = \Psi_z' i_d \,. \tag{3}$$

Therefore, The flux linkage per axial displacement Ψ_z' is equal to the current force factor. The *d*-axis current and *q*-axis current can generate axial suspension force and torque, respectively. Moreover, suspension force and torque can be obtained by voltage equation parameters.

3. Magnetic circuit

In this section, voltage equation parameters are mathematically derived by the permeance method. In the proposed motor structure, the flux goes through not only on *xy* plane but also on *xz* plane because proposed structure have three layers in the rotor PMs and in the stator. Therefore, magnetic circuits are considered in both *xz* and *xy* planes to derive the voltage equation parameters.

3.1 Equivalent magnetic circuit in *xz* cross-sectional view

Fig. 4 shows equivalent magnetic circuit in *xz* cross-sectional view. The magnetic circuit is estimated by flux distributions in the 3D-FEM analysis. To simply the calculation, let us assume that permeability in the stator core is infinite and magnetic saturation can be neglected. A ground symbol indicates that the magnetic potential is equal to zero. Let us define that the radial air gap length and the axial air gap length as l_{gR} and $l_{gA,}$ respectively. The rotor PMs outer radius is r_m. The radial thickness of rotor PMs is t_m. The axial length of center and side rotor PMs are l_{mc} and l_{ms}, respectively. The axial air gap length l_{gA} is equal to the axial length of side PMs l_{ms}. The reluctance in the center layer PM is R_{mc}. The reluctance in side layer PMs is R_{ms}. The air gap reluctance at center layer is R_{gc}. The flux per pole at the center, upper, and lower teeth are ϕ_c , ϕ_{su}, and ϕ_{sl}, respectively. The A_c and A_s indicate the magnetic potentials at the each rotor layer. Let us define μ_0 and B_r as a permeability of vacuum and residual magnetization of PM, respectively. The Magneto-Motive-Force (MMF) A_m in the rotor PMs can be given by

$$A_m = \frac{B_r t_m}{\mu_0} \,. \tag{4}$$

Fig. 5 shows an enlarged magnetic circuit around upper gap in Fig. 4. The reluctance per pole $R_{gu}(z)$ and $R_{gl}(z)$ in the upper and lower gaps are expressed with a radial reluctance component R_{gsR} and axial upper and lower reluctance components $R_{guA}(z)$, and $R_{glA}(z)$. The axial reluctance components depend on the rotor axial positon z. The equivalent reluctance of the upper gap and lower gap R_{gs} can be given by

$$R_{gs}(z) = R_{gu}(z) // R_{gl}(z) \,. \tag{5}$$

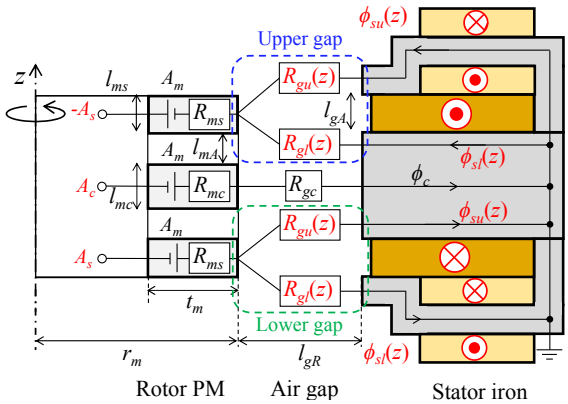

Fig. 4. Equivalent magnetic circuit in *xz* cross-sectional-view.

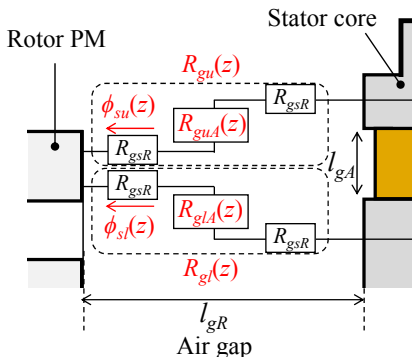

Fig. 5. Enlarged view of upper gap.

3.2 Equivalent magnetic circuit in *xy* cross-sectional view

Fig. 6 shows flux density distribution in *xy* cross-sectional view. The PM fluxes pass through the air-gap, and circulate in the stator core and come back to the rotor PMs.

Fig. 7 shows the equivalent magnetic circuit in the *xy* cross-sectional view. The equivalent magnetic circuit is

estimated from the flux distribution in the 3D-FEM analysis. To simplify the calculations, the stator core is approximated to a ring yoke core without teeth. In addition, the MMF distribution is supposed to be sinusoidal. In Fig. 7, the *xy* cross-sectional view of only one cycle of the electric angle is shown. The magnetic circuit inside of the rotor PM is just open because the rotor shaft is para-magnetic material. Therefore, the center layer rotor yoke reluctance R_{mcB} is given by the following equation with the correction coefficient *a*.

$$R_{mcB} = \frac{a\pi / p \cdot (r_m - t_m)}{\mu_0 l_{mc} (r_m - t_m)/2} = \frac{2a\pi}{p\mu_0 l_{mc}}. \tag{6}$$

In this manuscript, the correction coefficient *a* equal to 0.6 from the 3D-FEM analysis. In case of upper and lower layers, the equivalent magnetic circuit in *xy* cross-section can be expressed by replacements of the reluctances from R_{mc}, R_{gc}, and R_{mcB} to R_{ms}, R_{gs}, and R_{msB}, respectively. The upper and the lower layer rotor yoke reluctance R_{msB} is given by

$$R_{msB} = \frac{a\pi / p \cdot (r_m - t_m)}{\mu_0 l_{ms} (r_m - t_m)/2} = \frac{2a\pi}{p\mu_0 l_{ms}}. \tag{7}$$

From equivalent magnetic circuit in *xz* and *xy* plane, the rotor PMs flux per pole ϕ_c , $\phi_{su}(z)$, $\phi_{sl}(z)$ can be calculated as

$$\varphi_c = \frac{A_m}{R_{mc} + R_{gc} + R_{mcB}/4} \tag{8}$$

$$\varphi_{su}(z) = \frac{R_{gl}(z)}{R_{gu}(z) + R_{gl}(z)} \frac{A_m}{R_{ms} + R_{gs}(z) + R_{msB}/4} \tag{9}$$

$$\varphi_{sl}(z) = \frac{R_{gu}(z)}{R_{gu}(z) + R_{gl}(z)} \frac{A_m}{R_{ms} + R_{gs}(z) + R_{msB}/4}. \tag{10}$$

In Eq. (9) and (10), the rotor PM flux per pole $\phi_{su}(z)$ and $\phi_{sl}(z)$ depend on the rotor axial positon *z*.

Fig. 8(a) and (b) show the rotor PMs flux $\phi_{su}(z)$ and $\phi_{sl}(z)$ in Eq.(9) and Eq. (10) with respect to the rotor axial positon *z*. The flux per pole is greatly influenced by the axial air gap length l_{gA} and the side rotor PM axial length l_{ms}.

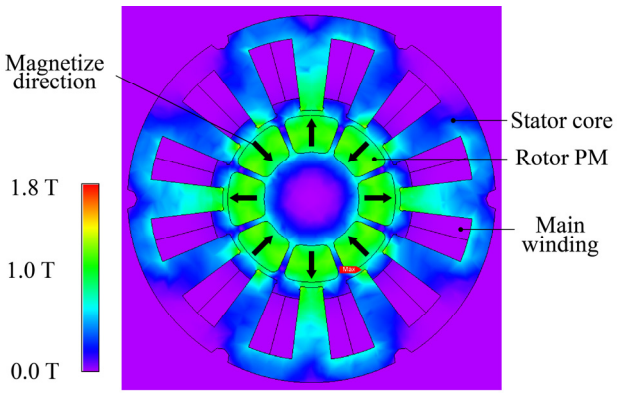

Fig. 6 Flux density distribution in *xy* cross-sectional view.

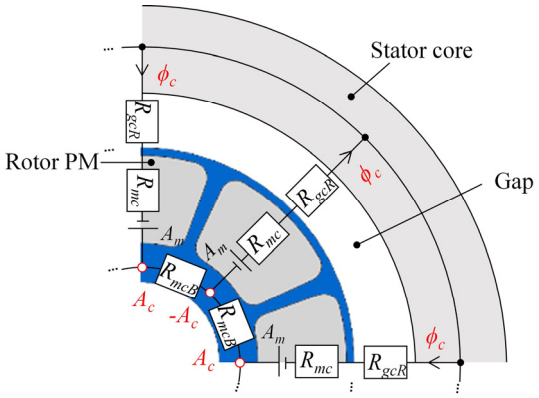

Fig. 7 Equivalent magnetic circuit in *xy* cross-sectional-view.

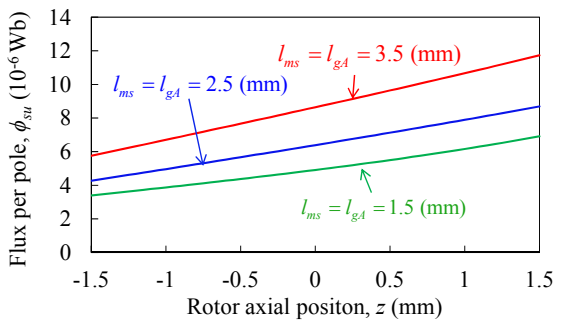

(a)

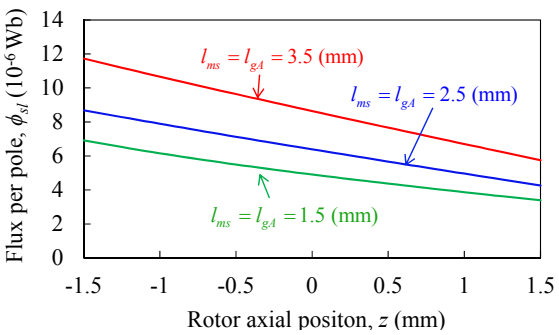

(b)

Fig. 8 The rotor PMs flux per phase ϕ_{su} and ϕ_{sl} with respect to rotor axial positon z.

3.3 Active axial force and torque

Let us define N_c and N_s as numbers of turns of main windings per phase and supplemental windings per phase, respectively. The flux linkage by the magnetic field is given by

$$\Psi_f(z) = \sqrt{\frac{3}{2}} N_c(\varphi_c + \varphi_{su}(z) - \varphi_{sl}(z)) + \sqrt{\frac{3}{2}} N_s(\varphi_{su}(z) - \varphi_{sl}(z)) = \sqrt{\frac{3}{2}} N_c \varphi_c + \sqrt{\frac{3}{2}}(N_c + N_s)(\varphi_{su}(z) - \varphi_{sl}(z)). \quad (11)$$

The flux linkage by the magnetic field at $z = 0$ is Ψ_ω. The derivative of the flux linkage with respect to z is Ψ_z'. Therefore, Ψ_ω and Ψ_z' are given as

$$\Psi_\omega = \Psi_f(0) = \sqrt{\frac{3}{2}} N_c \varphi_c = \sqrt{\frac{3}{2}} \frac{N_c A_m}{R_{mc} + R_{gc} + R_{mcB}/4} \quad (12)$$

$$\Psi_z' = \frac{\partial \Psi_f(z)}{\partial z} = \sqrt{\frac{3}{2}}(N_c + N_s)\frac{\partial}{\partial z}(\varphi_{su}(z) - \varphi_{sl}(z)) = \sqrt{\frac{3}{2}}(N_c + N_s)\left(\frac{\partial \varphi_{su}(z)}{\partial z} - \frac{\partial \varphi_{sl}(z)}{\partial z}\right) \quad (13)$$

4 Confirmation with FEM and Experimental result

Table. 1 shows geometrical and electrical parameters. In the calculations, only the axial gap length l_{gA} and the axial length l_{ms} of the rotor side PM are variable parameters. The stator diameter D_s, the rotor PMs outer diameter D_m, rotor PM thickness t_m, rotor center PM axial length l_{mc}, radial gap length l_{gR} and slot fill factor are fixed. The slot fill factor in *xy* and *xz* cross sections are 31% and 38%, respectively.

Fig. 9(a) and (b) show the *xz* cross-sectional view when the lengths l_{gA} and l_{ms} are short and long, respectively. The number of turns of main winding and supplemental winding are decreased in case of Fig. 9(a) because the slot area is decreased in the *xz* cross section. The number of turns of supplemental winding is only increased in case of Fig. 9(b) because the slot area in the *xy* cross section is not increased.

Fig. 10 and Fig. 11 compare the current-force factor Ψ_z' and rated torque T, respectively, with respect to the axial gap l_{gA} by the permeance method and 3D-FEM analysis, respectively. Moreover, an experimental result is plotted in Fig. 10. The torque and current-force factor are calculated by Eq.(2), (3), (12), and (13). The calculation results are approximately corresponding with that of the 3D-FEM analysis in magnetically unsaturated region. The experimental result is also close to the calculated curve.

5 Conclusion

The equivalent magnetic circuits have been proposed for the single-drive bearingless motor. The mathematical calculation by a permeance method is presented. It is confirmed that calculated active axial force and torque are corresponding with that of 3D-FEM analysis. In addition, it is found that the calculated active axial force is close to the measured force obtained from experimental results with a test machine.

Table 1. Geometrical and electrical parameters.

Parameter	Symbol	Unit	Value
Geometrical			
Stator outer diameter	D_s	mm	58
Rotor PM outer diameter	D_r	mm	26.4
Rotor PM thickness	t_m	mm	5.7
Rotor center PM axial length	l_{mc}	mm	2.8
Rotor PM axial space	l_{mA}	mm	2.1
Radial magnetic gap	l_{gR}	mm	0.8
Electrical			
Rated RMS current	I_0	A	1
Current density	J	A/mm^2	8
PM residual magnetization	B_r	T	1.28

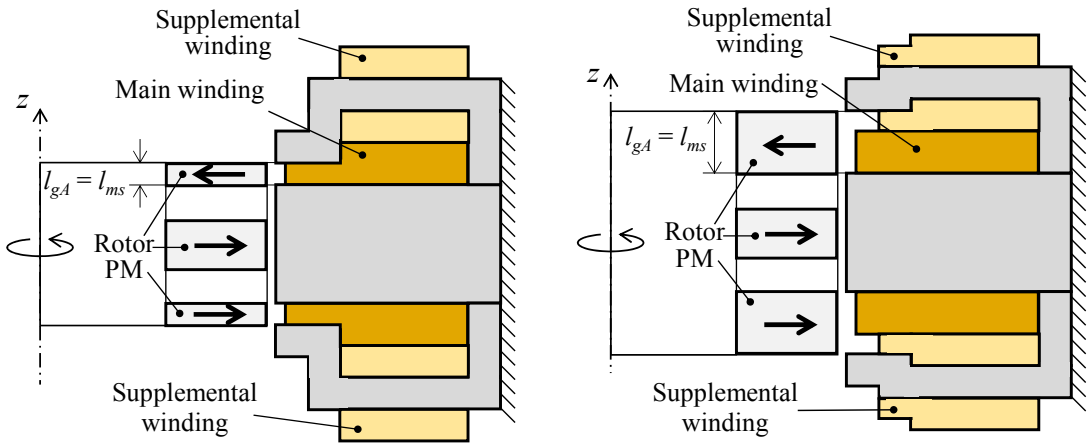

(a) l_{gA} and l_{ms} are short. (b) l_{gA} and l_{ms} are long.

Fig. 9 The *xz* cross-sectional view when axial gap length l_{gA} and rotor side PM axial length l_{ms} have changed.

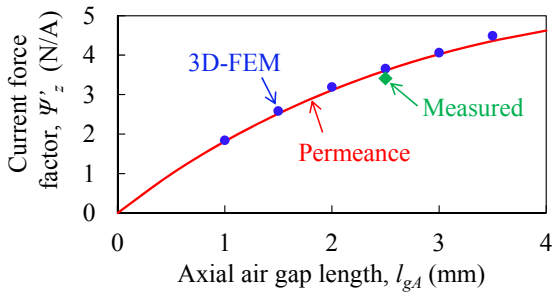

Fig. 10 Current force factor Ψ'_z with respect to axial gap length l_{gA}.

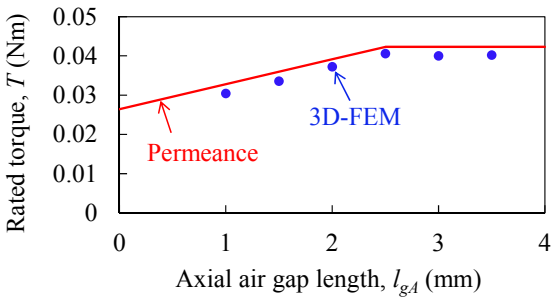

Fig. 11 Rated torque with respect to axial gap length l_{gA}.

Acknowledgment

This work supported by JSPS KAKENHI Grant Numbers 16H02324.

References

[1] J. Kuroki, T. Shinshi, L. Li, and A. Shimokohbe, “A micro-magnetic bearing using capacitive axial displacement sensing”, *Precis. Eng.*, vol. 30, no. 1, pp. 54–62, Jan. 2006.

[2] Q. D. Nguen and S. Ueno, “Modeling and control of salient-pole permanent magnet axial-gap self-bearing motor”, *IEEE/ASME Trans. Mechatronics,* vol. 16, no. 3, pp. 518–526, Jun. 2011.

[3] W. Bauer and W. Amrhein, “Electrical Design Considerations for a Bearingless Axial-Force/Torque Motor”, *IEEE Trans. Ind. Appl.*, vol. 50, no. 4, pp. 2512–2522, July/August 2014.

[4] I. D. Silva, J. R. Cardoso, and O. Horikawa, “Design Considerations for Achieving High Radial Stiffness in an Attraction-Type Magnetic Bearing With Control in a Single Direction”, *IEEE Trans. Magn.*, vol. 47, no. 10, pp. 4112–4115, Oct. 2011.

[5] T. Ohji, Y. Katsuda, K. Amei and M. Sakui, “Structure of One-Axis Controlled Repulsive Type Magnetic Bearing System With Surface Permanent Magnets Installed and Its Levitation and Rotation Tests”, *IEEE Trans. Magn*., vol. 47, no. 12, pp. 4734-4739, Dec. 2011.

[6] J. Asama, Y. Hamasaki, T. Oiwa, and A. Chiba, “Proposal and Analysis of A Novel Concept of a Single-Drive Bearingless Motor", *IEEE Trans. Industrial Electronics*, vol. 60, no. 1, pp. 129-138, Jan. 2013.

[7] H. Sugimoto, I. Shimura, and A. Chiba, “Design of SPM and IPM Rotors in Novel One-Axis Actively Positioned Single-Drive Bearingless Motor”, *in Proc. Energy Convers. Congr. and Expo.* (*ECCE2014*), pp. 5858-5863, 2014.

[8] H. Sugimoto, I. Shimura, and A. Chiba, “A Novel Stator Structure with Soft Magnetic Composite in One-Axis Actively Positioned Single-Drive Bearingless Motor”, *in Proc. Energy Convers. Congr. and Expo.* (*ECCE2015*), pp.2821-2827, 2015.